

RESEARCH ARTICLE

Temporal and spatial variations of convection, clouds and precipitation over the Tibetan Plateau from recent satellite observations. Part II: Precipitation climatology derived from global precipitation measurement mission

Julia Kukulies¹ | Deliang Chen¹  | Minghuai Wang²¹Regional Climate Group, Department of Earth Sciences, University of Gothenburg, Gothenburg, Sweden²School of Atmospheric Sciences, Nanjing University, Jiangsu, Nanjing, China**Correspondence**

Deliang Chen, Department of Earth Sciences, University of Gothenburg, PO Box 460, SE-405 30 Gothenburg, Sweden.
Email: deliang@gvc.gu.se

Funding information

Chinese Academy of Sciences, Grant/Award Number: XDA2006040103; National Natural Science Foundation of China, Grant/Award Numbers: 41575073, 41621005, 91537210, 91744208; Swedish Foundation for International Cooperation in Research and Higher Education, Grant/Award Number: CH2015-6226; Swedish National Space Agency, Grant/Award Number: SNSA: 188/18 4; Vetenskapsrådet, Grant/Award Numbers: 2014-5320, 2017-03780; Ministry of Science and Technology of China, Grant/Award Number: 2017YFA0604002

Abstract

This sequence of papers examines spatio-temporal variations of precipitation over the Tibetan Plateau (TP) based on satellite observations. Here in Part 2, spatial patterns of seasonal and diurnal variations of precipitation have been examined based on the Global Precipitation Measurement Mission (GPM) and three additional satellite products. The results show a spatial dipole pattern of two distinct seasonalities: The central TP is marked by strong July peaks and exhibits rainfall contributions of the monsoon season (May–September) of more than 70%, whereas northwestern and southern regions of the plateau exhibit significantly smaller amplitudes in the annual cycle. In some southern regions which are characterized by very high summer mean precipitation and more extreme rain rates, winter months (October–April) contribute significantly to the total annual mean precipitation. In addition, there are larger differences in seasonal curves along a west-to-east axis, than along a north-to-south axis. The spatial patterns of diurnal precipitation over the TP are more complex compared to seasonality and point to multiple components, which construct the regional differences. These show also a seasonal dependence and are characterized by a stronger afternoon to early evening peak (17:00 LST time, 11:00 UTC) and weaker nighttime peak (23:00 LST, 17:00 UTC) during the monsoon season and over the plateau compared to its surroundings. Furthermore, it was shown that convective precipitation during the monsoon season contribute only up to 30% to the total precipitation, whereas more than 70% is produced by the 90th percentile of daily rain rates. An important characteristic of summer precipitation is hence that a significant part of the extreme precipitation is non-convective. This paper reveals new features of spatial

This is an open access article under the terms of the Creative Commons Attribution License, which permits use, distribution and reproduction in any medium, provided the original work is properly cited.

© 2020 The Authors. International Journal of Climatology published by John Wiley & Sons Ltd on behalf of the Royal Meteorological Society.

patterns in seasonal and diurnal precipitation and highlights the importance of non-monsoonal components for seasonal precipitation variations.

KEYWORDS

convective precipitation, diurnal cycle, GPM, monsoon, principal component analysis, seasonality, Tibetan Plateau

1 | INTRODUCTION

The Tibetan Plateau (TP) is also referred to as the Third Pole, because it stores the largest amounts of fresh water after the Arctic and Antarctica (Yao *et al.*, 2018). With an average elevation above 4,000 m a.s.l. over an area of 5 million km² (Yao *et al.*, 2018), it is the most extensive high altitude region of the world. It represents also one of the most sensitive regions to climate change, because intensive surface heating which is reinforced by different feedback mechanisms lead to enhanced atmospheric warming, glacier retreat and an accelerated hydrological cycle (Bibi *et al.*, 2018).

Precipitation is a key parameter for hydro-climatic changes in the TP region (Bibi *et al.*, 2018), which is why precipitation variability and its relationship to the large-scale atmospheric circulation have been addressed for a long time (Flohn and Reiter, 1968; Luo and Yanai, 1983). Precipitation climatologies have been derived from ice core reconstructions (Yao *et al.*, 2013), ground measurements, satellite observations, reanalysis data (Tong *et al.*, 2014) and downscaled climate model simulations (Maussion *et al.*, 2014). Due to inherent limitations of different observations and resolution issues in model simulations, the results can exhibit highly deviating values for precipitation amounts (You *et al.*, 2015), whereas some patterns appear to be consistent in most of the data sets:

In general, the TP is characterized by a wet summer season and dry winter season related to mid-latitude westerlies and Indian summer monsoon (Zhang *et al.*, 2017), as well as a diurnal cycle with nighttime precipitation peaks (Fujinami *et al.*, 2005; Liang *et al.*, 2010; Bao *et al.*, 2011; Xu and Zipser, 2011). Whereas most of the studies agree on an overall wetting trend, the strong dependence of precipitation on elevation and on different sources of moisture transport (Chen *et al.*, 2015; Yao *et al.*, 2018), the regional variations and different mechanisms which control precipitation regimes at different scales are yet not fully understood. One reason for this is the complex topography of the TP, which leads to uncertainties in precipitation estimates from the sparsely distributed rain gauges (Gao *et al.*, 2015) and wet biases in both observations and model simulations (Lin *et al.*, 2018).

One important precipitation-producing mechanism in the TP region is the formation of meso-scale convective systems (MCS), which can reach horizontal dimensions larger than 300 km (Maddox, 1980; Feng *et al.*, 2014). Because these originate partly from the TP and are partly transported by large-scale circulation systems towards the plateau (Maddox, 1980), MCS exhibit both seasonal (Hu *et al.*, 2016) and regional variations (Hu *et al.*, 2017). The linkages between precipitation, large-scale circulation, topography and local convection are current research questions which need to be explored.

In order to investigate convection dynamics and its importance for precipitation over the TP, it is first important to create a robust climatology of prevailing cloud and precipitation patterns, which reveal general variations of convection in the region. Since cloud microphysics and cloud vertical structure are directly linked to precipitation formation, the purpose of this paper sequence is to simultaneously cast some light on spatio-temporal variations of cloud properties and precipitation and to create a climatology from satellite missions which complement each other in terms of temporal resolution and retrieved parameters. Whereas Part 1 (Kukulies *et al.*, 2019) focused on differences of cloud micro- and macrophysical properties in three subregions of the TP, which are affected differently by large-scale atmospheric circulation and moisture transport (westerly-dominated domain, transition zone, monsoon-dominated domain), this paper aims to complement the findings by presenting the spatio-temporal variations of precipitation with a focus on regional differences of seasonality and diurnal variations. The reason for analysing spatial patterns of precipitation at these temporal scales is to elucidate multiple components of precipitation variations. In order to get a better understanding of how these components interact with each other, we aim to identify regional and seasonal dependencies of precipitation characteristics, such as diurnal maximum, convective and extreme precipitation.

Moreover, we focus on satellite retrievals from the Global Precipitation Measurement Mission (GPM), since data products such as GPM IMERG are available at a high spatial and temporal resolution and combined microwave and infrared observations. To put these

observations in a perspective of other high resolution multi-sensor satellite products of precipitation, the climatologies are also compared to CMORPH, TRMM (3B42) and MSWEP.

The paper is structured as follows: Section 2 briefly presents the satellite data sets and methods, which were used to identify spatial patterns of temporal variations in precipitation. In Section 3, seasonal variations in the different datasets and spatial patterns of seasonality are presented. Section 4 focuses on diurnal precipitation variations and its regional/seasonal dependencies and Section 5 examines additional features of seasonal precipitation, namely, extreme and convective precipitation. In Section 6, the findings from this part of our paper sequence are summarized and discussed in the context of large-scale atmospheric circulation and convective systems. We also discuss retrieval uncertainties and inherent technical limitations and give recommendations for future studies of precipitation in the TP region based on satellite observations. The key findings and conclusions are summarized in Section 7.

2 | DATA AND METHODOLOGY

2.1 | Satellite data

The GPM Core Observatory (Hou *et al.*, 2014) consists of a passive and an active sensor, which measure hydrometeors in near-real time. It orbits the globe between 65°S to 65°N within 93 min (on average 16 times per day) and lies in a near-equatorial orbit at an altitude of 407 km. It has thus a revisit time of 1–2 hr and is able to capture diurnal variations of different precipitation types. The passive satellite sensor GPM Microwave Imager (GMI) has an increased number of microwave channels and frequency range compared to its predecessor TMI of the Tropical Rainfall Measurement Mission (TRMM). In addition, the Dual-Frequency Precipitation Radar (DPR) of the GPM Core Observatory operates at two frequencies (Ka-band at 35.33 GHz and Ku-band at 13.6 GHz) and allows for the record of vertical hydrometeor profiles

with a large range of particle sizes, since it provides additional information about the droplet size distributions of snow and rain. It has also a larger capacity of detecting snow and light rainfall and is thus more suitable for high latitude and altitude environments in comparison to single-frequency precipitation radars (Kulie and Benartz, 2009).

The different data products of GPM, which have been used in this study are listed in Table 1. GPM IMERG provides a uniform and gauge-calibrated dataset including observations from more than 20 precipitation sensors of TRMM/GPM and comprehensive databases of microwave brightness temperatures as well as vertical hydrometeor profiles from various passive and active satellite sensors (Huffman *et al.*, 2015b). Due to the improved algorithm for high latitude and altitude regions and the high temporal resolution, GPM IMERG appears to be most promising among the GPM data products. The IMERG algorithm merges precipitation estimates from microwave measurements with microwave-calibrated infrared (IR) observations and rain gauges, in order to produce a global gridded product at a high spatial and temporal resolution. We use here version 05 of the IMERG “final run”, which incorporates monthly gauge data and is in particular produced for scientific purposes (Huffman *et al.*, 2015b). In addition, we used the daily gridded dataset GPM 3GPROF, which is based on DPR and provides convective vs. stratiform precipitation fractions.

For Mainland China, different satellite rainfall products have been evaluated (Zhou *et al.*, 2008; Tang *et al.*, 2016), whereby GPM IMERG reproduces probability density functions and diurnal cycles of precipitation which are closest to station measurements (Tang *et al.*, 2016). Moreover, Xu *et al.* (2017) showed that GPM IMERG reduces the well-known wet bias in precipitation observations over the TP and outperforms the Tropical Rainfall Measurement Mission (TRMM) for this specific region. However, because GPM data is only available from 2014 and covers hence a short time period, GPM IMERG was compared to three other global high-resolution precipitation products, which also merge measurements from multiple satellite sensors, but use different algorithms for

TABLE 1 Overview of GPM data and other multi-sensor satellite products used in this study

Data product	Parameters	Reference	Resolution	Period
GPM IMERG v05	Column-integrated gauge-calibrated precipitation	Huffman <i>et al.</i> (2015b)	0.1°, 30 min	2014–2017
GPM 3GPROF	Convective precipitation fraction	Iguchi <i>et al.</i> (2010)	0.25°, daily	2014–2015
TRMM 3B42	Calibrated surface precipitation (IR and microwave)	Kummerow <i>et al.</i> (1998)	0.1° × 0.25° 3 hr	2014–2017
MSWEP	Weighted surface precipitation estimate	Beck <i>et al.</i> (2017)	0.1°, 3 hr	2014–2016
CMORPH-CRT	Surface precipitation estimate	Joyce <i>et al.</i> (2004)	8 km, 30 min	2014–2017

the final estimates (Table 1): TRMM (3B42), CMORPH (CRT) and MSWEP (Multi-Source Weighted-Ensemble Precipitation). All used datasets were chosen at the highest spatial and temporal resolutions available, in order to get an accurate representation of diurnal and regional variations.

While TRMM and CMORPH have been used in several studies of precipitation over the TP (Gao and Liu, 2013; Maussion *et al.*, 2014; Tang *et al.*, 2016; Xu *et al.*, 2017), the recently created global dataset MSWEP is used for the first time for the TP region. In this datasets, optimal precipitation estimates are created based on multiple satellite observations combined with both ground-based measurements and reanalysis data, whereby the different data sources are merged based on weight maps. For example, in a region like the TP, where gauge observations are sparse, more weight is given to satellite observations and reanalysis data. It should be noted, that the three datasets used are not completely independent. Even though these are constructed from different retrieval algorithms and data assimilation systems, they also share information: MSWEP includes, for instance, TRMM and CMORPH in the final precipitation estimate.

2.2 | Precipitation variations in the study domain

Figure 1a displays the DEM of the TP domain. In this study, the TP domain is constraint to all locations (pixels) within this domain above 3,000 m ASL. It is also the domain chosen for the regionally averaged metrics describing precipitation variations, in order to focus on the high elevation region of the TP and to exclude regions south of the plateau, because these are strongly affected by the Indian summer monsoon and would therefore dominate the signals for the entire domain (cf. sec. 3). We refer to this domain (27–45°N, 70–105 °E) as the “TP” when only elevations above 3,000 m ASL are included and to “TP + surrounding” when the surrounding lower elevations within the domain are included.

Figure 1b highlights the strong topographic variation, which can occur over small areas over the TP and especially in the northwest and along the steep slopes of the southern foothills (up to 1,400 m standard deviation within 3 km grid cells).

In Part 1 of this paper sequence (Kukulies *et al.*, 2019), variations of cloud characteristics based on cloud profiles were compared between three subregions of the TP, which are affected differently by large-scale atmospheric circulation. Here, we chose to examine the spatial patterns of seasonality, diurnal variations and extreme/

convective precipitation over the entire TP instead of regions with predefined boundaries, since the high-resolution gridded data allow (in contrast to the cloud profiles) for a more accurate identification of regional differences.

In order to detect new regional patterns than the known north–south differences (Yao *et al.*, 2013; Maussion *et al.*, 2014), we performed a principal component analysis (PCA) on both seasonal and diurnal variations of precipitation over the TP. To identify the spatial patterns of temporal variations rather than actual variations in precipitation intensity, precipitation rates were first normalized by calculating the monthly (hourly) contributions in % to total annual (daily) precipitation. The input feature space for the PCA, was thus the normalized seasonal (diurnal) vector for each grid cell in the domain displayed in Figure 1a (n grid cells \times 12 monthly/24 hr precipitation contributions). The corresponding output is the eigenvector strengths for each grid cell, which indicates the deviation from the mean conditions of the dataset and can be used to reconstruct the first and second principal components of the seasonal and diurnal vectors. This is done by adding the eigenvector strengths to the per feature mean (seasonal/diurnal vector) and multiply it by the principal axis in feature space for the highest (first principal component) and second highest (second principal component) explained variance. This allows for the identification of regions or clusters of locations with distinct principal components for seasonal variations of precipitation (e.g., due to different large-scale atmospheric circulation impacts).

3 | SEASONALITY

The monthly contributions to the total annual mean precipitation for the four satellite data products averaged over the TP domain are displayed in Figure 2. It can be seen that the seasonal curves exhibit the same shape and similar monthly fractions in all data sets. This shows the robustness of the facts that the regional precipitation over the TP has a distinct peak with the highest contributions from June – August and that the monsoon season from May – September contributes to more than 70% to the total annual precipitation. GPM IMERG exhibits the highest contribution during the monsoon season (80%) despite the fact that mean rain rates are lower than in the other datasets (Figure 3).

The average precipitation rates (mm/day) during the monsoon season May – September show also similar spatial patterns in the four datasets (Figure 3). There is a distinct northwest-southeast diagonal with the highest mean precipitation rates occurring in the southeastern

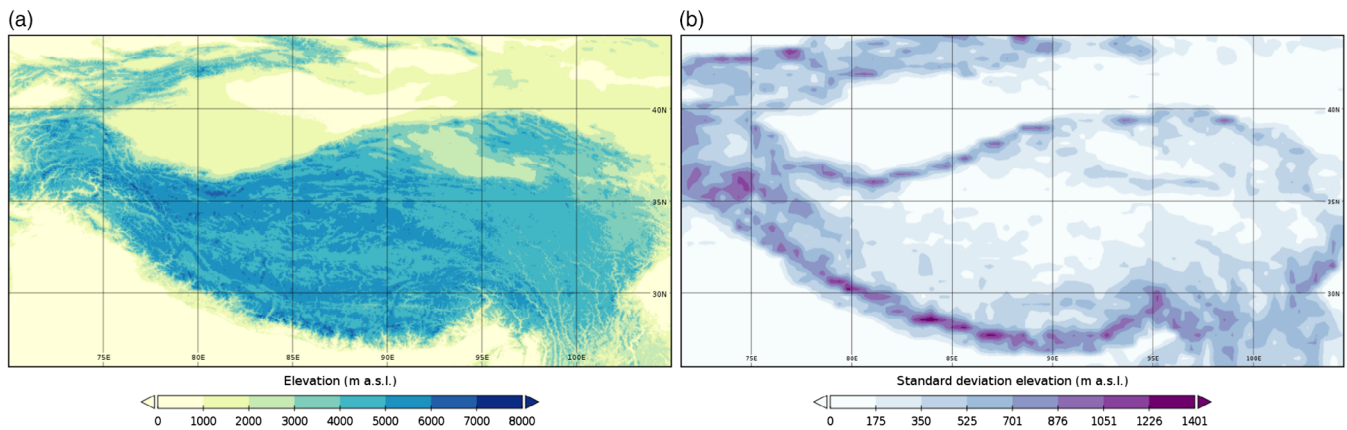


FIGURE 1 Topography of the Tibetan plateau (TP) based on 30 m resolution data from the shuttle radar topography Mission (SRTM). (a) Displays a DEM of the TP and surrounding region. Locations within the domain 27–45°N, 70–105°E and above 3,000 m ASL are in this study defined as the TP. (b) Shows the standard deviation of elevation in every 3 km × 3 km grid. (a) DEM of the TP and surrounding region (b) variation of elevation over the TP [Colour figure can be viewed at wileyonlinelibrary.com]

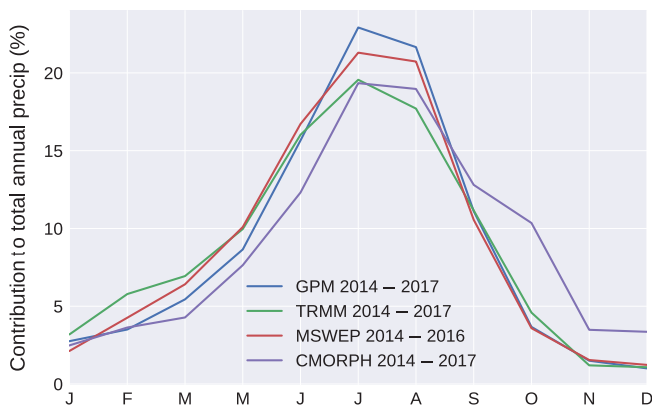


FIGURE 2 Monthly contributions to total annual mean precipitation (%) for GPM, CMORPH, TRMM and MSWEP. The seasonal curve shows the average over the TP domain for the years 2014–2017 of GPM, CMORPH, and TRMM and 2014–2016 for MSWEP [Colour figure can be viewed at wileyonlinelibrary.com]

TP. Outside the 3,000 m boundary, the most extreme precipitation occurs south of the Himalayas. In addition, there is a region in the northwest outside of the plateau, which is marked by higher precipitation rates compared to the surroundings, which is clearly visible in all datasets (Figure 3). In general, MSWEP has the latter two features most pronounced and the highest precipitation rates over the plateau. This might be due to the incorporation of reanalysis data, which has a known wet bias for the high altitude region of the TP (Gao *et al.*, 2015; Lin *et al.*, 2018). In addition, MSWEP is the only dataset that has daily rain rates during May – September exceeding 10 mm-day⁻¹ within the 3,000 m boundary of the plateau (Figure 3).

Even though it has long been recognized that the monsoon season dominates the temporal variations over

the plateau (which is also clearly visible in Figure 2), the regional differences of variations in the seasonal cycle are not established. Figure 4 shows that some of the mountain ranges stretching from the northwest to southwest receive a significant part of the precipitation between October and April, when mid-latitude westerlies rather than the monsoon circulation dominates the atmospheric water vapour transport (Yao *et al.*, 2013; Liu *et al.*, 2016). This region, where the contribution of summer precipitation between May and September only contributes with less than 30% to the total annual precipitation, accords very well among TRMM, MSWEP and GPM (Figure 4). In the CMORPH data, the pattern looks slightly different and the lower summer precipitation contributions are rather constraint to the northeast of the northwestern mountain ranges. To get clearer picture of the regions within the TP in which the seasonal cycle of precipitation is controlled by other factors than the monsoon circulation, we examined the first two principal components of the normalized seasonality (Figures 5 and 6).

Figure 5 shows the sign and strengths of the first principal component (PC1), which explains 52.8% of the variance in the GPM data. In other words, the colours indicate how much the seasonal curves in each grid cell deviate from the regionally averaged seasonal precipitation. The red regions are characterized by a distinct summer precipitation peak, whereas the blue regions have significant monthly contributions to annual precipitation outside of the monsoon season. In order to demonstrate the main features of seasonal precipitation in the two opposing regions, the seasonal curves at two locations (A and B) with extreme eigenvector strength values are shown in comparison to the part of the curves, which are explained by PC1 at the respective

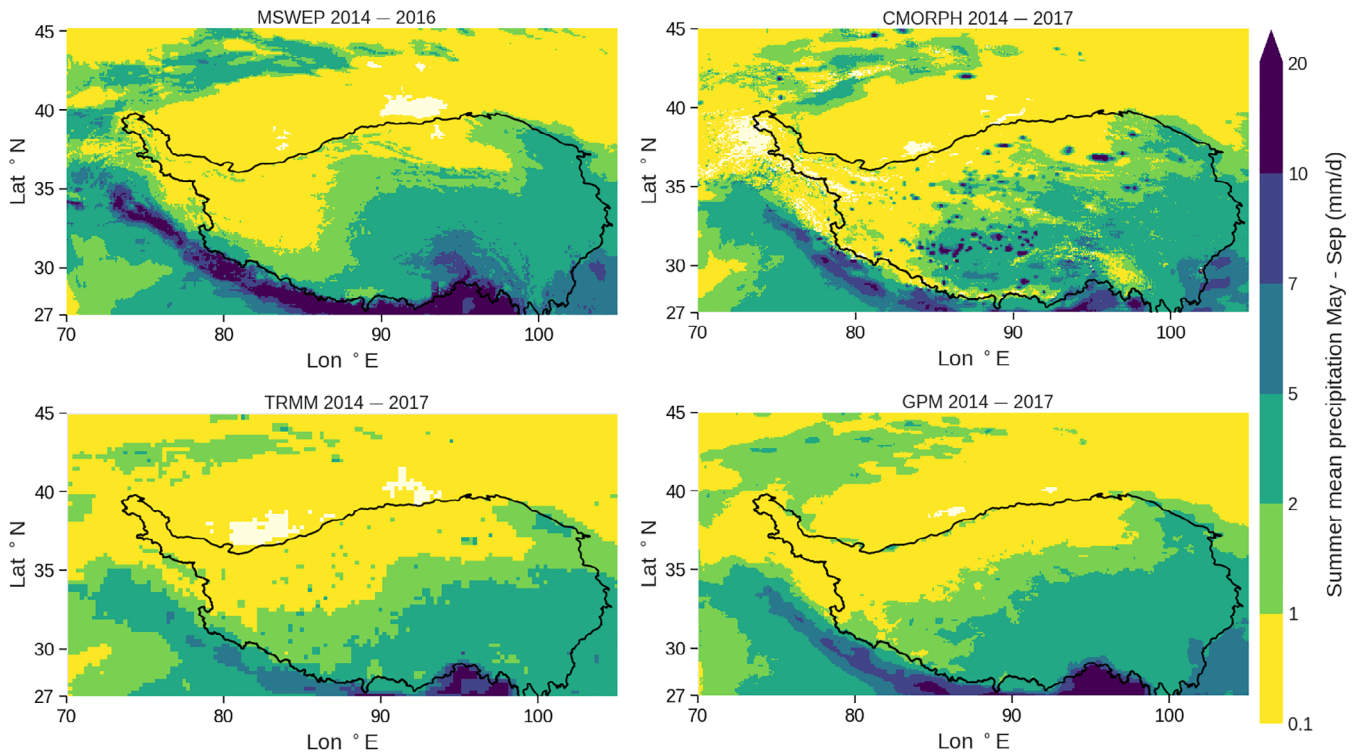


FIGURE 3 Mean precipitation rates ($\text{mm}\cdot\text{day}^{-1}$) during May–September for MSWEP (2014–2016), CMORPH (2014–2017), TRMM (2014–2017) and GPM (2014–2017) [Colour figure can be viewed at wileyonlinelibrary.com]

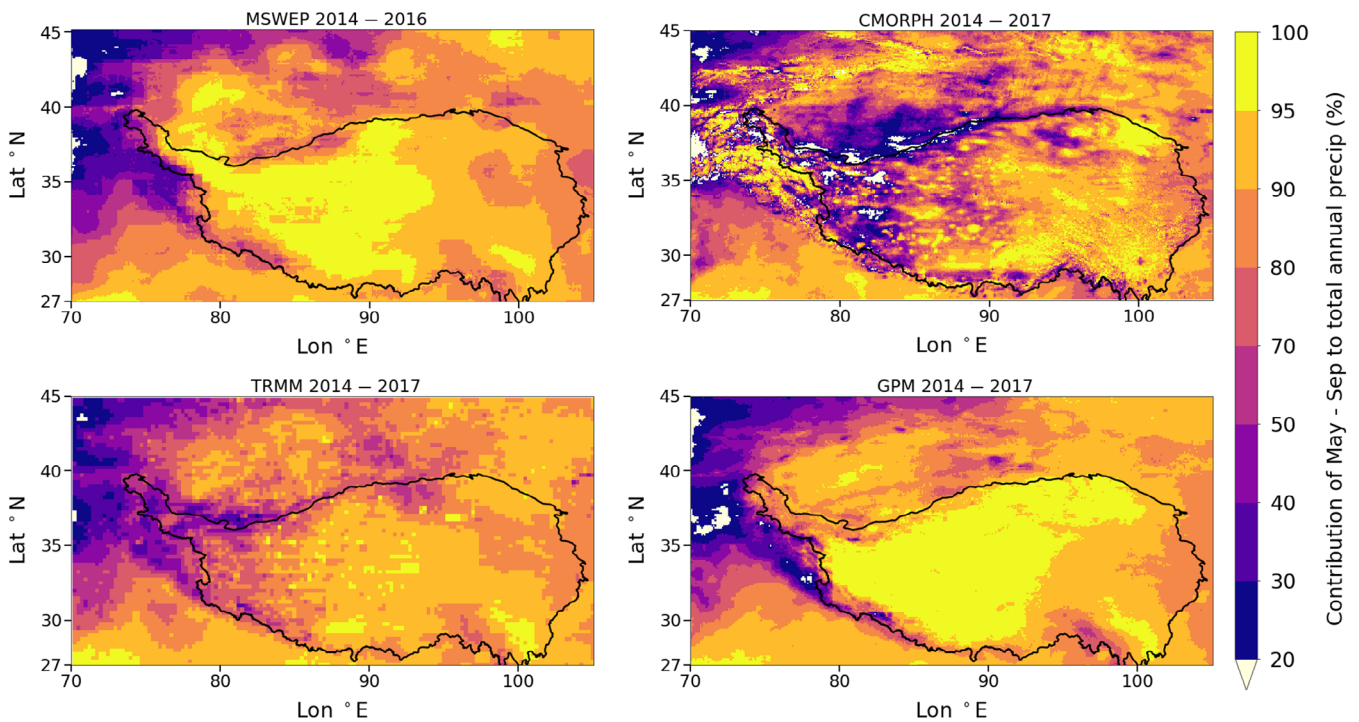


FIGURE 4 Contributions of summer precipitation (May–Sep) to total annual mean precipitation (%) for MSWEP, CMORPH, TRMM and GPM. The seasonal curve shows the average over the TP domain for the years 2014–2017 of GPM, CMORPH and TRMM and 2016–2016 for MSWEP [Colour figure can be viewed at wileyonlinelibrary.com]

FIGURE 5 First principal component (PC1) of the normalized annual cycle over the TP, which explains 52.8% of the variance in the GPM data. The colours red and blue indicate the sign and strength of the eigenvectors of PC1. The PC1 of variations in monthly contributions to total annual mean precipitation (2014–2017) are shown for two example locations a and B (solid lines), which are marked by different PC1 of seasonality. In addition, the actual seasonal curves at the respective locations (dashed lines) are displayed in comparison to the regionally averaged seasonal curve for the TP domain (black line) [Colour figure can be viewed at wileyonlinelibrary.com]

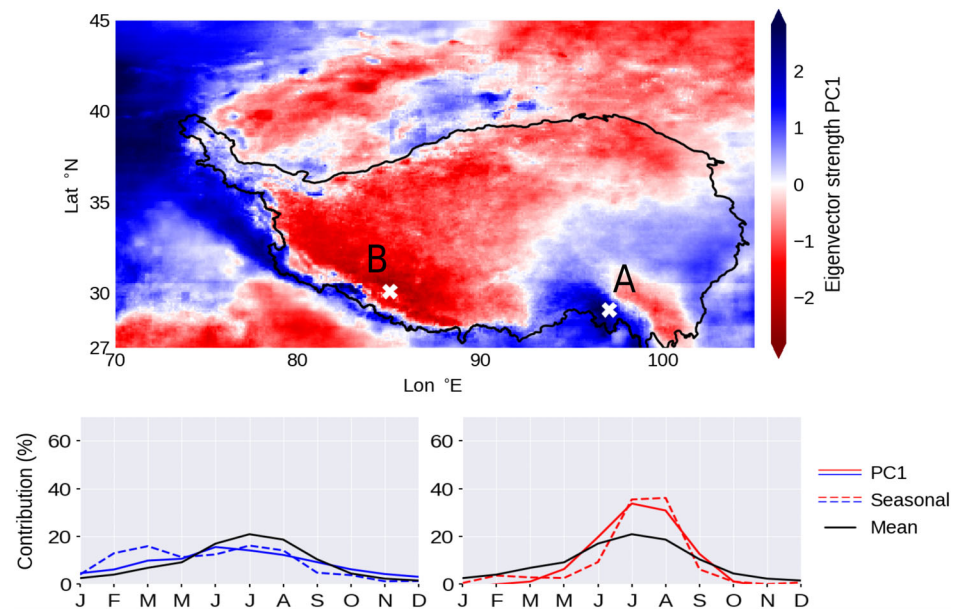
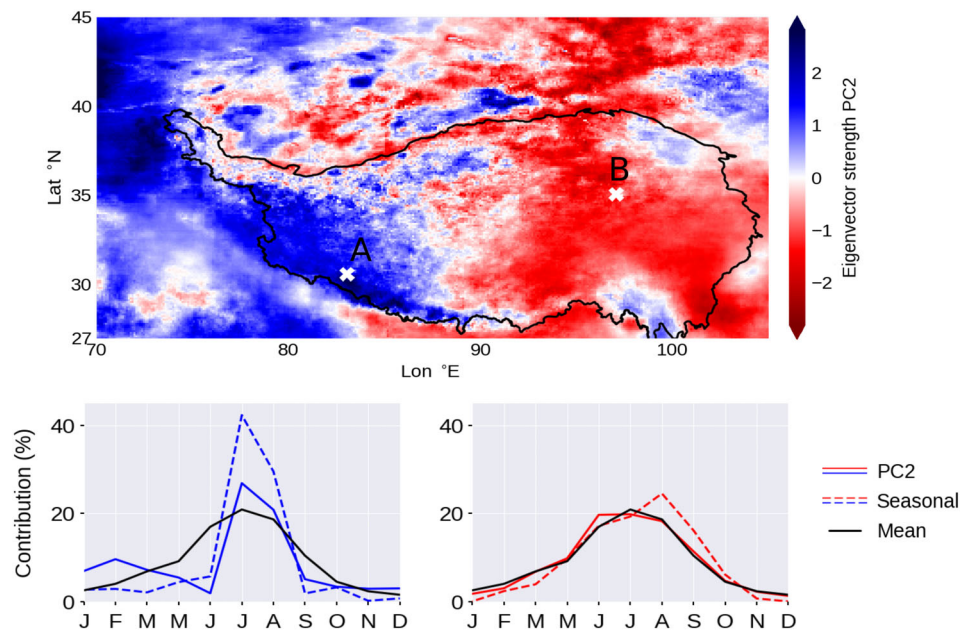


FIGURE 6 Second principal component (PC2) of the normalized annual cycle over the TP, which explains 21.8% of the variance in the GPM data. The colours red and blue indicate the sign and strength of the eigenvectors of PC1. The PC1 of variations in monthly contributions to total annual mean precipitation (2014–2017) are shown for two example locations a and B (solid lines), which are marked by different PC1 of seasonality. In addition, the actual seasonal curves at the respective locations (dashed lines) are displayed in comparison to the regionally averaged seasonal curve for the TP domain (black line) [Colour figure can be viewed at wileyonlinelibrary.com]



location (Figure 5). Locations A and B are chosen from the 90th percentile of positive (blue) and negative (red) eigenvector strength values in the plateau region. The black line in Figure 5 shows the regionally averaged curve over the entire domain (TP + surroundings), to visualize how much the seasonal curves at the example locations A and B (dashed lines) can deviate from regionally averaged seasonal curve. The solid lines display the two contrasting features of the PC1 for blue (example point A) and red (example point B) regions: The PC1 for regions with

strong negative eigenvector strength is marked by a distinct summer peak and the PC1 of regions with strong positive eigenvector strength values is marked by a flatter seasonal curve. The points reveal, hence, an interesting feature of the southern parts of the TP: The “blue” pattern (which represents a higher contribution during the winter months compared to the red regions) expands along the southern mountain ranges towards the southeastern edges of the TP. This means that the seasonal variation in some parts of the southeastern strongly resembles the northwest outside of the plateau.

Comparing Figures 5 and 3, it becomes clear that the blue regions are marked by relatively high precipitation rates during summer. Hence, the flatter seasonal curves do not indicate the absence or smaller impact of the monsoon circulation, but rather the additional influence of other large-scale atmospheric circulation systems. Knowing that mid-latitude westerlies arrive from the northwest (here characterized by strong positive eigenvector strengths) and transport moisture to the plateau between October and April, the dipole pattern in Figure 5 suggests the far-reaching impact of westerlies.

While the PC1 explains the regional differences in seasonality between the major parts of the central plateau compared to the surrounding region and edges of the plateau, the second principal component (PC2), which explains 21.8% of the variance in the data, clearly divides the plateau into a western and an eastern region (Figure 6). The blue and red regions differ mainly due to a shift from a PC2 precipitation peak in July (blue) to a PC2 precipitation peak in August (red). To exemplify how seasonal curves in dark-blue and dark-red coloured regions can look like, we show again the seasonal curves and their corresponding PC2 at two locations A and B, which represent extreme positive (blue) and negative (red) eigenvector strength values.

The PC1 of the annual cycle revealed the feature of the seasonal cycle that explained most of the variance. This feature could, hence, be attributed to the large-scale atmospheric circulation, which has the most important impact on the shape of the seasonal curve. The physical interpretation of the second principal component is less straightforward. However, we can see a distinct east–west separation and the earlier summer precipitation peak in the west compared to the east could indicate the impact of the East Asian summer monsoon, which typically has a later onset than the Indian summer monsoon arriving from the Bay of Bengal (Yihui and Chan, 2005). Another possible mechanism for the shifted summer precipitation peak is the formation of MCS in the eastern TP due to an east–west heating contrast (Sugimoto and Ueno, 2010), since MCS also can contribute to large portions of summer precipitation (Hu *et al.*, 2016).

Summarizing the results from the PCA, the first two principal components of the seasonal cycle together explain ca. 75% of the variance in the data and show clear dipole patterns even within the higher elevations of the TP (e.g., differences along the southern mountain range). The two distinct spatial clusters revealed by the first principal component are regions with a clear summer peak contrasted by regions with more moderate seasonal variations. Another important finding, which expands previous knowledge about variations in seasonal precipitation over the TP, is that the west-to-east differences which are

shown by both the first and the second principal components seem to be more dominant compared to the previously recognized north-to-south differences. This indicates more complex patterns of the impact of large-scale atmospheric circulation on seasonal precipitation than simple north-to-south regimes.

4 | DIURNAL VARIATIONS

Figure 7 displays the normalized diurnal cycles of GPM, CMORPH, TRMM and MSWEP separated into two seasons (May–September and October–April) based on 30 min data for GPM and CMORPH (Figure 7a,b) and 3 hr data for TRMM and MSWEP (Figure 7c,d). In order to highlight the role of elevation for the diurnal cycle, the dashed lines display the diurnal cycles for the TP (27–45°N, 70–105°E) when the lower elevated surroundings are included (TP + surrounding). All datasets show smaller amplitudes in the diurnal curves when lower elevated surrounding regions are included and larger precipitation contributions during nighttime hours. CMORPH exhibits earlier diurnal precipitation peaks compared to the other datasets, whereby the diurnal curves for the two seasons show also remarkable differences (Figure 7b). While GPM, MSWEP and TRMM show a clear evening peak during both seasons (around 17:00 local solar time, 11:00 UTC), CMORPH shows a noon and afternoon peak from October to April and an afternoon as well as an evening peak (15:00 and 20:00 local solar time, 09:00 and 14:00 UTC) from May to September. All datasets agree, however, on the clear valley around 12:00 local solar time (04:00 UTC), except for CMORPH during the dry season (Figure 7b).

While the regionally averaged curves in Figure 7 do not reveal any significant seasonal differences (except for CMORPH), the more detailed spatial patterns of diurnal maximum precipitation show clear differences between the wet and dry season (Figure 8). During the wet season (May–September), the western plateau is dominated by maximum precipitation in the afternoon to early evening (15:00–18:00 local solar time), while the eastern plateau exhibits earlier afternoon precipitation maxima between 12:00 and 15:00 local solar time. Maximum precipitation in the time slots 15:00–18:00 and 21:00–00:00 local solar time occur at many locations of the plateau during this season, as was depicted in Figure 7a. Lower elevated terrains, for example, at the leeward side of the Himalayas, are marked by maximum precipitation during nighttime in the wet season (Figure 8). During the dry season (Oct–Apr) the spatial distribution of diurnal precipitation maxima shows a generally more patchy pattern, so that it is difficult to distinguish any larger regions which is

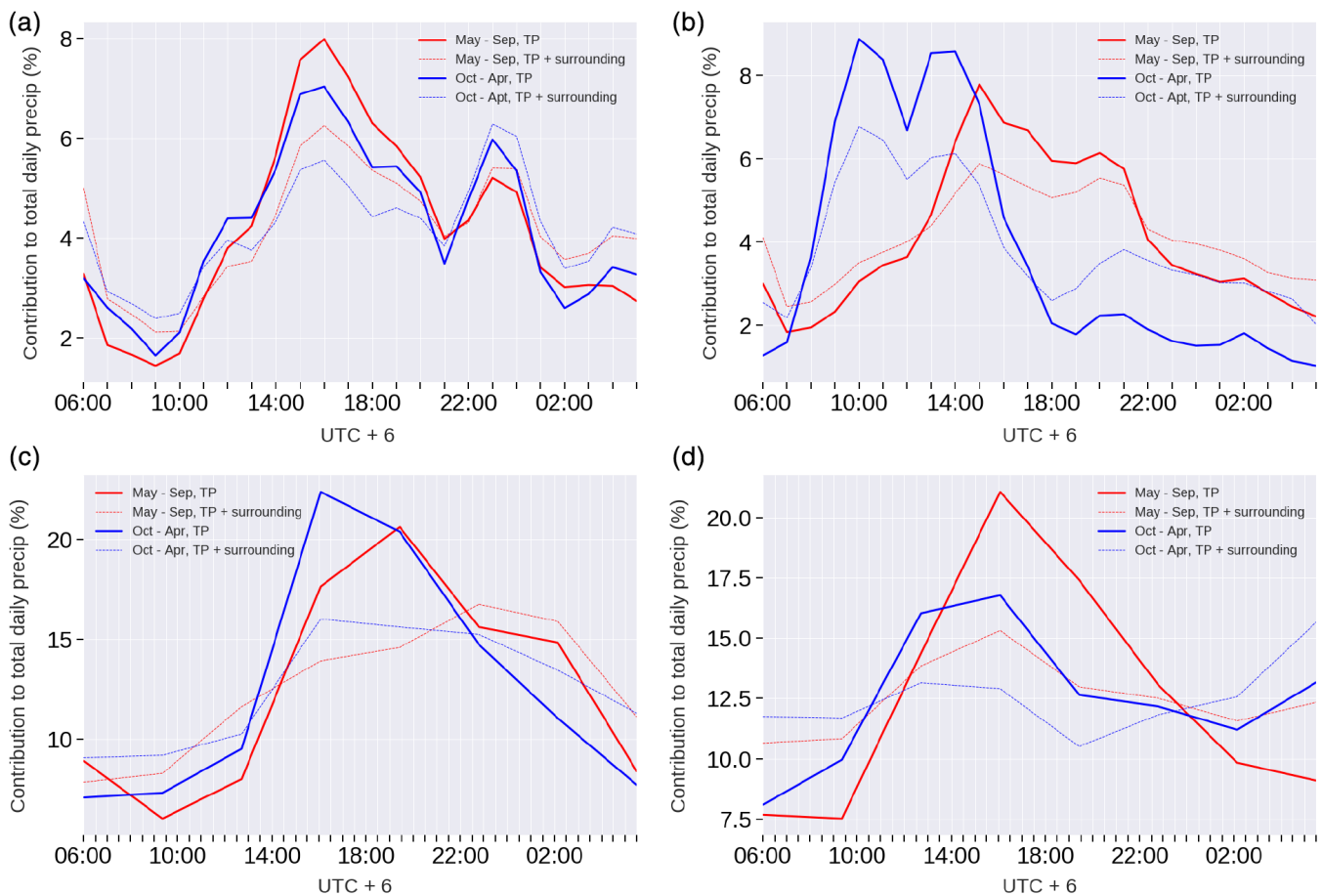


FIGURE 7 Diurnal cycle of surface precipitation over the TP for (a) GPM (2014–2017), (b) CMORPH (2014–2017), (c) TRMM (2014–2017) and (d) MSWEP (2014–2016). The relative contributions to the total daily precipitation amount in % are based on 30 min data for GPM and CMORPH and 3 hourly data for TRMM and MSWEP. The dashed lines display the diurnal curves averaged over the entire domain (27–45°N, 70–105°E) including surrounding regions at lower level elevations. The curves are further divided into two seasons: May–September (red) and October–April (blue) [Colour figure can be viewed at wileyonlinelibrary.com]

marked by the same maxima. Only the northwestern plateau stands out by shifting the early evening—evening precipitation peak to a peak in the early morning with maximum precipitation between 06:00 and 09:00 local solar time (Figure 8).

The differences between the wet and dry seasons in Figure 8) show clearly that spatial patterns of diurnal variations are seasonally dependent, even if the regionally averaged diurnal curves of the two seasons look similar (Figure 7a). This indicates that seasonal, diurnal and regional precipitation patterns are not strictly independent from each other due to interactions of precipitation mechanisms at different scales. For instance, the fact that we can distinguish regional patterns of maximum precipitation in the wet season demonstrates that the monsoon circulation is an important component for diurnal variations. A possible explanation for this is the large-scale moisture transport, which enables and enhances interaction with topography in different regions simultaneously.

In addition, meso-scale convective systems, which form from intensive surface heating, also have a typical diurnal cycle (Li *et al.*, 2008) and could thereby affect diurnal precipitation variations at a larger scale. Diurnal variations during the dry season are, by contrast, more controlled by local processes due to the absence or synoptic and meso-scale forcings.

To further investigate systematic regional differences of diurnal precipitation, we also performed a PCA on hourly contributions to the total daily precipitation amount (Figure 9). The first principal component of diurnal cycles over the TP can only explain 34.4% of the GPM data, which indicates that diurnal variations over the TP have in general many additional components. This underlines the importance of smaller scale precipitation processes for the diurnal cycle in complex mountain terrains.

The pronounced dipole pattern, which is visualized by the red vs. blue regions, shows that the TP within the

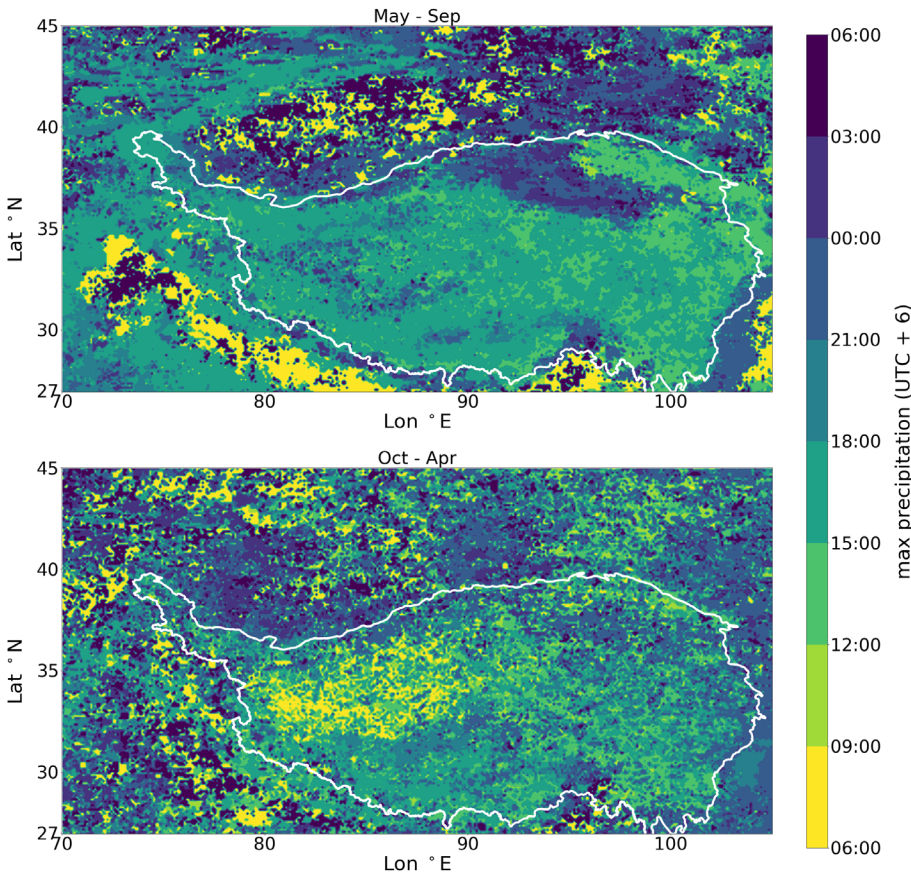


FIGURE 8 Local solar time (UTC + 6) of diurnal maximum precipitation over the TP based on GPM IMERG (2014–2017) for wet (May–Sep) and dry (Oct–Apr) season [Colour figure can be viewed at wileyonlinelibrary.com]

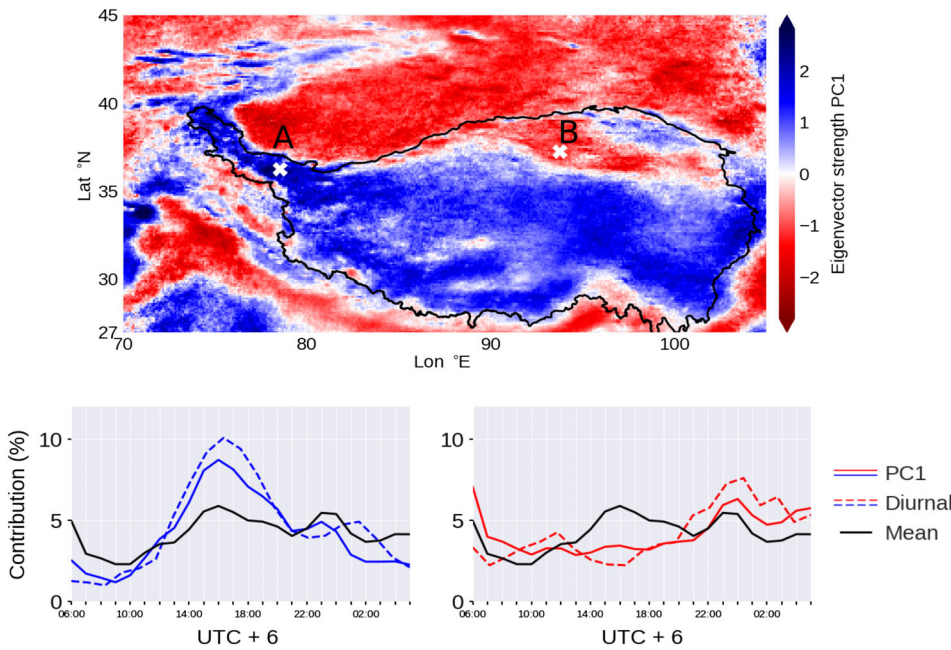


FIGURE 9 First principal component (PC1) of the normalized diurnal cycle over the TP, which explains 34.4% of the variance in the GPM data. The colours red and blue indicate the sign and strength of the eigenvectors of PC1. The PC1 of variations in hourly contributions to total daily mean precipitation (2014–2017) are shown for two example locations a and B (solid lines), which are marked by different PC1 of diurnal variations. In addition, the actual seasonal curves at the respective locations (dashed lines) are displayed in comparison to the regionally averaged seasonal curve for the TP domain (black line) [Colour figure can be viewed at wileyonlinelibrary.com]

3,000 m boundary distinguishes from the lower elevated surrounding regions (Figure 9). The two distinct regional clusters become even more apparent in Figure 10 which shows the histograms of the

eigenvector values for PC1 of diurnal variations for TP + surrounding regions (Figure 10a) compared to TP (Figure 10b). While the entire domain including surrounding regions at lower level elevations exhibits a

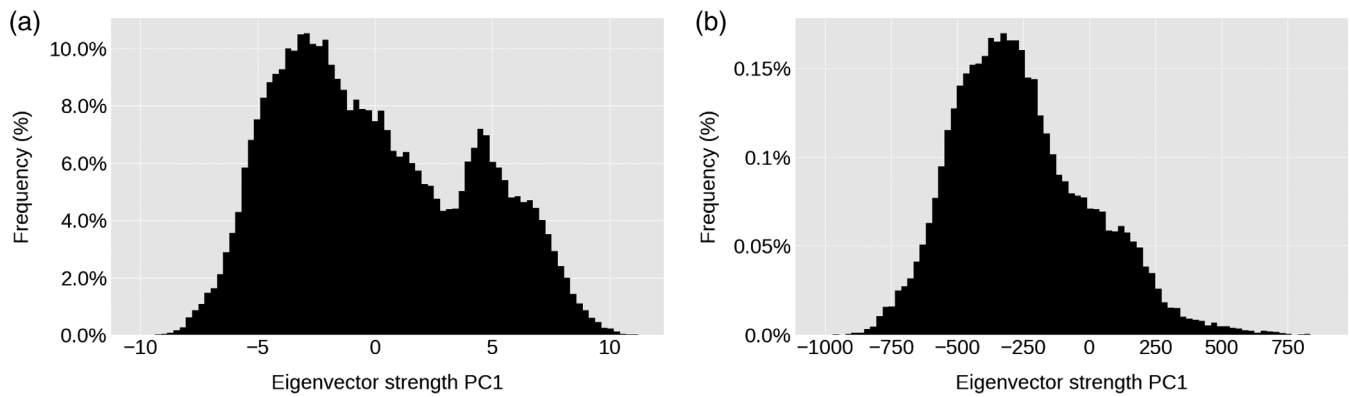


FIGURE 10 Histograms of the first principal component of diurnal variations for (a) the TP and the lower elevated surrounding regions and (b) the TP domain

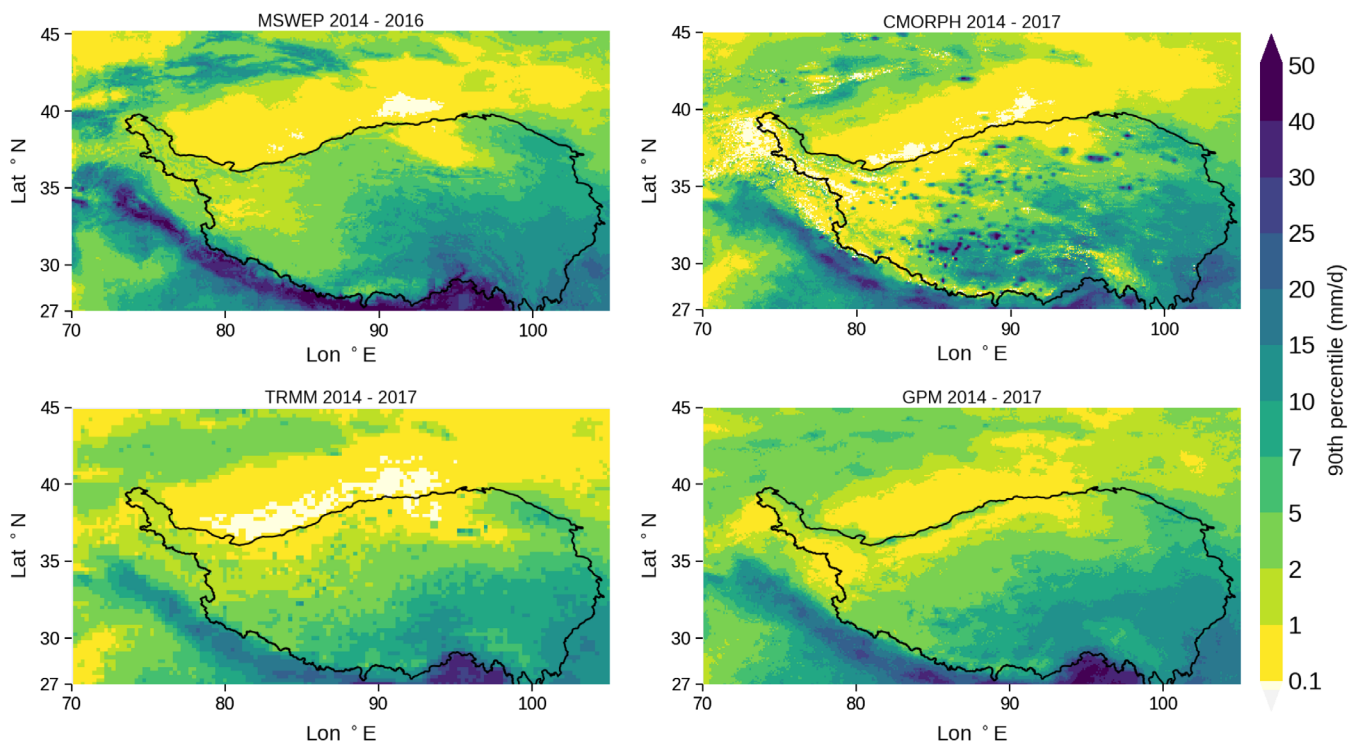


FIGURE 11 90th percentile of daily rain rates during May–Sep for MSWEP, CMORPH, TRMM and GPM. The 90th percentile has been calculated for the years 2014–2017 of GPM, CMORPH and TRMM and 2014–2016 for MSWEP [Colour figure can be viewed at wileyonlinelibrary.com]

distinct bimodal distribution, the TP (at elevations above 3,000 m ASL) is marked by a unimodal distribution for PC1 eigenvector values. This means that clear clusters of diurnal variations are only visible when the lower elevated surrounding regions are included, which again underlines the dependence of precipitation patterns on elevation and topography.

In Figure 9, we show the diurnal cycles and their corresponding first principle components of two example points with strong eigenvector strength values of opposite

sign (same as Figures 5 and 6). It can be seen that PC1 at location A manifests an afternoon– early evening peak (17:00 local solar time, 11:00 UTC), which is clearly higher than the average diurnal curve of the TP + surrounding domain. At point B, which is used as an extreme example for dark red coloured regions, the diurnal curve deviates even more from the regional average. Here, the diurnal cycle is characterized by a late evening (06:00 local solar time, 00:00 UTC) and early morning peak (23:00 local solar time, 17:00 UTC).

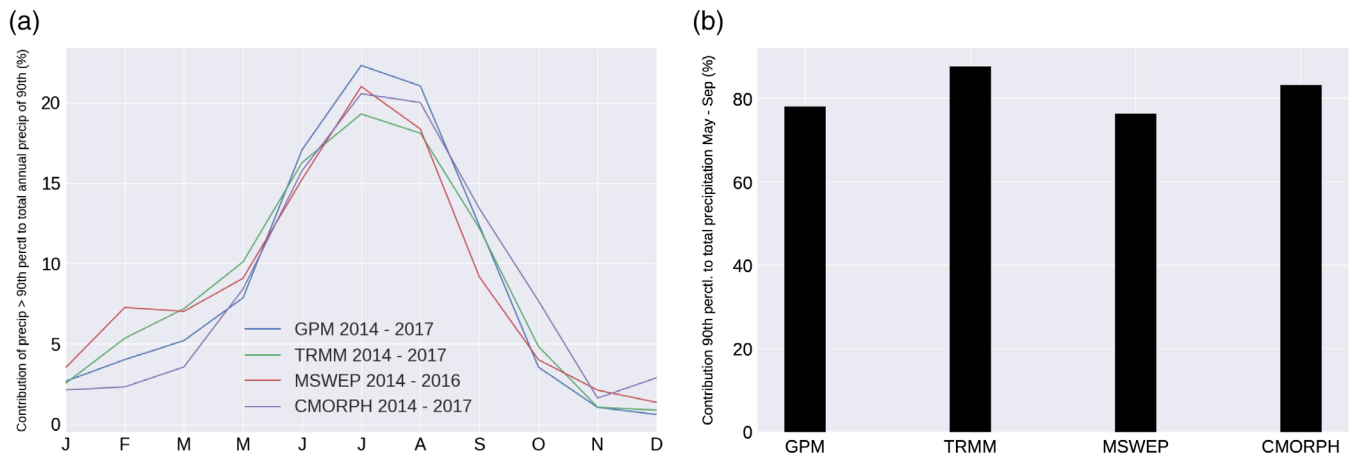


FIGURE 12 Extreme precipitation in GPM (2014–2017), TRMM (2014–2017) and MSWEP (2014–2016) and CMORPH (2014–2017). (a) Contribution of monthly 90th percentile daily precipitation to total monthly precipitation. (b) Contribution of total 90th percentile daily precipitation to total summer precipitation (May–September) [Colour figure can be viewed at wileyonlinelibrary.com]

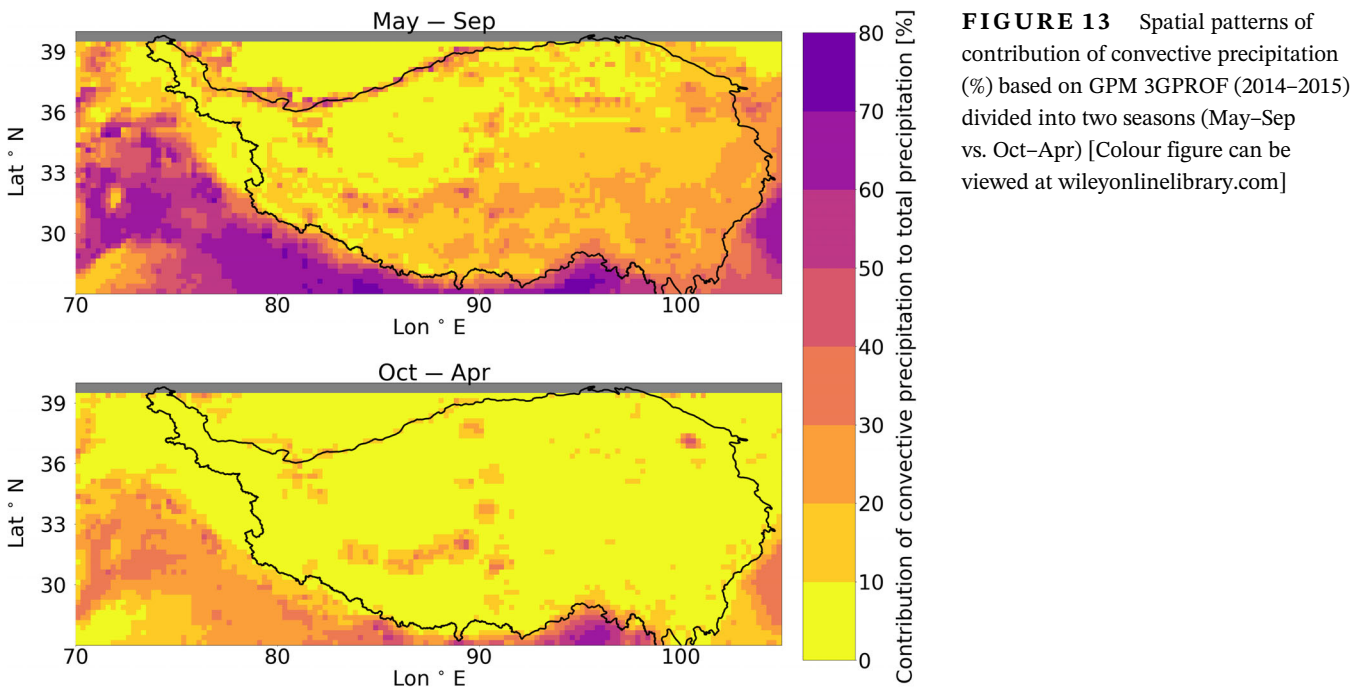


FIGURE 13 Spatial patterns of contribution of convective precipitation (%) based on GPM 3GPROF (2014–2015) divided into two seasons (May–Sep vs. Oct–Apr) [Colour figure can be viewed at wileyonlinelibrary.com]

5 | EXTREME PRECIPITATION

Having identified major spatio-temporal features of mean rain rates, it should be noted that these patterns do not necessarily coincide with patterns of heavy rain rates. For example, the southern regions of the TP are strongly blue-coloured in Figure 5 and exhibit therefore a rather flat seasonal curve even though the region is marked by high mean precipitation rates (Figure 3). That means that regions with similar mean rain rates during summer (Figure 3) but seasonal curves with a pronounced summer peak (Figure 5) experience more extreme rain rates

during only a few months of the year (mostly between May and September).

Figure 11 shows the spatial distribution of the 90th percentile of daily summer precipitation. The figure reveals that over the TP, indeed, the patterns are quite similar to total mean summer precipitation (Figure 3). Interestingly, the eastern parts of the southern mountain ranges (around 95 °E), which are marked by significant precipitation contributions outside of the monsoon season (Figure 5), also are the regions which experience the most extreme rain rates during summer (Figure 11).

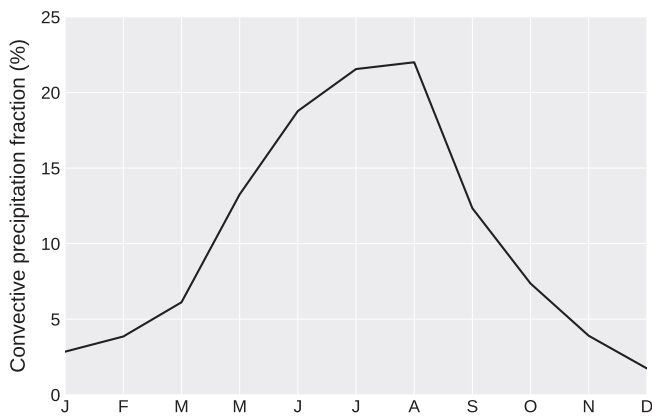


FIGURE 14 Annual cycle of convective precipitation fraction (%) based on GPM 3GPROF (2014–2015) averaged over TP (>3,000 m ASL)

Furthermore, the monthly total precipitation from daily rain rates above the regionally averaged 90th percentile to total monthly precipitation exhibits the same shape as monthly contributions to total annual mean (Figure 12a). This underlines firstly that most of the extreme precipitation occurs between May and September and secondly that most of the summer precipitation is produced by extreme precipitation. The total amount of precipitation produced by 90th percentile rain rates during the summer months (May – Sep) stands for around 80% of the total summer precipitation in all four datasets (Figure 12b).

6 | CONVECTIVE PRECIPITATION

Figure 13 shows the seasonal contributions of convective precipitation to the total precipitation based on DPR in the high-resolution 3GPROF product for 12 months from 2014 to 2015. Whereas only a small part of precipitating pixels (0 to 10% for most of the grid cells) is classified as convective between October and April, the contribution of convective precipitation varies between 10 and 40% in the eastern TP between May and September. The annual cycle of convective precipitation follows the same curve as for total precipitation (Figure 2) and shows a pronounced peak during the summer months with more than 80% of convective precipitation occurring between May and September (Figure 14). The seasonal difference indicates that convective precipitation is closely related to the monsoon circulation and is even more pronounced south of the TP, where the contributions of convective precipitation are between 60 and 80%. This is understandable as development of convection also needs moisture, which can be provided by the monsoon winds. The results verify that most of the convective precipitation

occurs south of the Himalayas, but the north to south gradient suggested in (Maussion *et al.*, 2014) is less visible and instead the west to east difference seem to be more pronounced in 3GPROF product. Further, this previous study showed that between 70% and 80% of the precipitation is of convective type in the central TP and up to 100% in the Himalayas (Maussion *et al.*, 2014). The contribution of convective precipitation based on 3GPROF is hence significantly lower than the previous study (Figures 13 and 14), which suggests that the role of convection (in both the westerly and monsoon season) for precipitation needs further consideration.

7 | DISCUSSION

7.1 | Precipitation and convection

Referring back to the key findings of Part 1 of this paper sequence (Kukulies *et al.*, 2019), the GPM-derived precipitation climatology confirms that stratiform cloud systems and stratiform precipitation occur frequently over the plateau. This was shown by the higher frequency of stratiform and ice cloud layer types and the radar reflectivity profiles in Part 1 and is here visible through relatively low contribution of convective precipitation all year round (Figure 13). Compared to insights about convective precipitation from the downscaled WRF product *High Asia Reanalysis* (HAR) (Maussion *et al.*, 2014), the contribution of convective precipitation estimated by GPM is significantly lower (Maussion *et al.*, 2014). However, it should also be noted that convection can occur at different scales and that the satellite convective precipitation fraction relies primarily on the horizontal and vertical structure of the radar signal (Kummerow *et al.*, 2001), whereas the convective precipitation in HAR data refers to the precipitation fraction produced by the cumulus parametrization scheme.

Since a significant part of precipitation-producing MCS occurs during the monsoon season (Maddox, 1980; Hu *et al.*, 2016, 2017), this suggests that the convective precipitation is probably partly associated with these MCS, but that the accompanied stratiform precipitation in MCS stands for much larger portion of precipitation. This is also reinforced by the fact that a large part of extreme precipitation during summer seems to be non-convective (Sections 5 and 6).

Further, the nighttime precipitation peaks south of the Himalayas suggest clearly that MCS can significantly affect the diurnal cycle of precipitation, since such systems produce usually most of the precipitation at night as they mature (Li *et al.*, 2008; Xu and Zipser, 2011). It is not trivial to separate effects of topography on the

incoming monsoon flow from heating-driven MCS south of the Himalayas, which both represent mechanisms that could affect diurnal precipitation. However, MCS are an example for how seasonally dependent weather systems (Hu *et al.*, 2016) also interact with local processes (such as topography-forced upslope winds) and thereby affect diurnal cycles of precipitation. The different spatial patterns of diurnal maximum precipitation in the different seasons (Figures 7 and 8) suggest that regional, seasonal and diurnal controls of precipitation interact with each other and are all important components of precipitation.

The GPM data indicate that precipitation occurrences between October and April can, despite their generally very low rain rates, significantly contribute to the total precipitation occurring along a stretch from northwest to the southern mountain ranges of the plateau. The analysis of the first two principal components of seasonal precipitation suggests that non-monsoonal contributions significantly affect precipitation along the southern and northwestern edges of the TP. In Part 1 of this paper sequence, it was found that the large-scale moisture transport by mid-latitude westerlies does not only control convection regimes in the northern TP domain but also in the central regions of the transition zone (Kukulies *et al.*, 2019). The precipitation climatology in this study also shows clearly that seasonal precipitation variations are not constraint to the north–south regionalization. This is consistent with Curio and Scherer (2016) who investigated precipitation dynamics over the TP based on HAR and found that despite the regional and seasonal variations of precipitation-producing mechanisms, the westerly circulation affects precipitation over the entire plateau and is not only limited to the northern region.

The PCA of diurnal precipitation revealed that the diurnal cycle has multiple components and less pronounced spatial patterns (or weaker explained variance of the principal components) compared to seasonal precipitation. This emphasizes the complexity of diurnal cycles of precipitation, since it can be caused by interaction of processes at many different scales. For example, elevation and topography can affect precipitation at different scales from more local mountain-plain solenoids (Zhang *et al.*, 2014) to large-scale elevation-dependence of precipitation (Li *et al.*, 2017). However, it should be noted that elevation-dependence is mainly controlled by two limiting factors: decreasing water vapour supply with elevation and increasing instability (Cuo and Zhang, 2017). Over the TP, the increasing instability has led to a general increase in summer precipitation with elevation up to ca. 4,000 m ASL, since enough water vapour can still be supplied in many regions (Cuo and Zhang, 2017). At higher elevations, precipitation amounts decrease due to an increasing lifting condensation level and

simultaneously decreasing humidity (Cuo and Zhang, 2017). On a diurnal scale, elevation effects are more local and complex in the way that no larger-scale spatial patterns are dominant within the 3,000 m boundary of the TP. Diurnal variations need hence to be studied in more detail under the consideration of local topography.

7.2 | Satellite data

Inter-comparison studies have shown that satellite observations of precipitation over the TP can exhibit large differences (You *et al.*, 2015; Wang *et al.*, 2017). This pertains in particular for precipitation parameters such as precipitation phase, which are highly dependent on retrieval algorithms (Iguchi *et al.*, 2010). Chen *et al.* (2016) quantified spatial scales of precipitation over the TP based on long-term satellite observations. They found that spatial coherences of precipitation show a strong dependence on directions, with the strongest correlations occurring along west–east. Further, the representativeness of precipitation at any given point typically decreased exponentially with distance and exhibited spatial scales between 111 and 182 km, which is only a third of the spatial scale of annual surface temperatures (Chen *et al.*, 2016).

Since the TP represents a high-altitude environment with very high variations of elevations over small distances (Figure 1b), generating distinct heating profiles and pressure fields, general assumptions of global satellite products like GPM (Elsaesser and Kummerow, 2015) do not accurately represent the specific atmospheric conditions over the TP. We aim therefore to give a short discussion on technical issues and recommendations for future studies of the TP based on satellite observations of precipitation and convection.

Because of the low temperatures, an important capability of satellite sensors used for TP studies is the detection of snow and solid precipitation. Compared to the CloudSat sensor CPR, the GPM sensor DPR has a lower sensitivity for frozen hydrometeors and a noise-reducing algorithm used for DPR might in some cases remove the radar signals from snow (Casella *et al.*, 2017). Whereas DPR alone captures approximately 30% of the total snow mass (Casella *et al.*, 2017), the aim of the GPM IMERG product is to improve the robustness for light rain and solid precipitation in mid-latitude regions by using multiple sensors with complementary skills (Huffman *et al.*, 2015a). However, the missing snow detection remains an issue despite improvements and could explain the very low precipitation amounts, which have been observed during the winter season in this study.

Retrieval algorithms for precipitation from passive microwave sensors (e.g., GMI) are highly dependent on scattering from ice particles (Xu *et al.*, 2017), which generally is an advantage for the TP, because it has high occurrence frequencies of ice and mixed-phase clouds (Kukulies *et al.*, 2019). However, the retrieval of precipitation type is more uncertain. Kirstetter *et al.* (2018) showed, for example, that GPM IMERG is able to capture the diurnal variability of precipitation at a regional scale, but highlight the concern that orographic and convective precipitation might be underestimated in high altitude regions. One reason for this misidentification has already been found in TRMM precipitation retrievals, where ground echo could be misidentified as melting layer of a stratiform cloud system, because the freezing level is close to the surface over the TP (Fu and Liu, 2007). It is therefore important to adequately address convective and stratiform precipitation over the TP in future studies, in order to determine whether the low contributions of convective precipitation in this study are due to technical errors or an indicator for other processes being more important for precipitation formation.

Compared to the Tropical Rainfall Measurement Mission (TRMM), GPM-retrieved precipitation rates tend to be closer to meteorological observations at ground-based stations of the TP (Xu *et al.*, 2017) and in contrast to the wet bias in regional climate models and reanalysis data for the TP (Su *et al.*, 2013; Gao *et al.*, 2015; Wang *et al.*, 2017) the main limitation of GPM is its larger missing ratio, especially for snow. Both the diurnal variations and total precipitation associated with the westerly moisture transport to the plateau might therefore be higher as presented here.

It should also be noted that the published GPM data products are only available for a short time period, in particular for the high-resolution data of GPROF (Table 1). In this study, it is assumed that the 3-year period from 2014 to 2017 can capture some of the general precipitation patterns (seasonal and diurnal variations) due to the high resolution. GPM IMERG does not have the capacity yet to accurately represent inter-annual variability, but the IMERG retrieval algorithms is currently under development and aims to extend its time period back to the start of the TRMM era in 1998 (Huffman *et al.*, 2015b). This prolonged time period will be object of more detailed future studies of precipitation over the TP.

Due to the inherent limitations of the satellite retrievals over the TP, we aim and recommend to improve retrieval algorithms for precipitation based on the ground radar stations over the TP (e.g., using ground-radar measurements as training data in machine

learning techniques), in order to account for the specific conditions of the region and minimize technical uncertainties. Ma *et al.* (2018) developed and evaluated a multi-satellite dataset created for precipitation retrievals for the specific region of the TP, by including the two widely used satellite precipitation datasets CMORPH and PERSIANN. However, this dataset has not been compared to any ground measurements yet, which underlines the need for the incorporation of ground-based observations. To pursue further studies of convective processes in the TP region and make best use of modern satellite observations, we recommend the use of ground-radars located in the TP for validation and improvements of cloud and precipitation retrievals from satellite observations.

We summarize therefore the most crucial aspects, which need to be addressed in future precipitation retrievals based on multi-satellites over the TP: (a) collocations to increase resolution and to reduce uncertainty, (b) accurate temperature profiles (e.g., for retrievals of cloud phase), (c) the reduction of ground clutter to improve the identification of stratiform and convective precipitation (d) and the calibration based on ground radars.

8 | CONCLUSIONS

This study investigated spatio-temporal variations of precipitation over the Tibetan Plateau (TP) based on the high-resolution satellite dataset GPM IMERG as well as three additional multi-sensor satellite products. The monthly contributions of total and extreme precipitation as well as the spatial patterns of summer mean and extreme precipitation mostly agree between the datasets. Diurnal cycles show some differences, but a clear valley around noon was visible in all datasets.

We used GPM IMERG to perform principal component analyses on normalized diurnal and seasonal precipitation over the TP.

The three key features of this analysis are:

1. The first principal component of seasonal variations shows a clear spatial dipole pattern for two distinct seasonalities: Major parts of the central TP are clearly marked by a seasonal curve which peaks in July and exhibits contributions of the monsoon season (May–Sep) of more than 70% to the total annual precipitation, whereas seasonal curves along the northwestern and southern edges of the plateau resemble those in northwestern regions outside of the plateau. Even in some southern regions which are characterized by very high mean summer precipitation and more

- extreme rain rates, winter months (Oct–Apr) contribute significantly to the total annual mean precipitation. Non-monsoonal components play, hence, an important even in some southern regions of the TP.
- The second principal component of seasonal precipitation reveals a west–east pattern, which emphasizes that large-scale differences in elevation affect seasonal precipitation. Since neither the first nor the second component shows a clear north–south pattern, we conclude that seasonal variations show larger regional differences on a west-to-east-axis.
 - Compared to spatial variations of seasonality, the spatial patterns of diurnal precipitation over the TP are more complex and point to multiple components which construct the regional differences. However, the TP stands out compared to its surrounding lower elevated areas with a strong early evening peak (17:00 local time, 11:00 UTC) and a weaker nighttime peak (23:00 local time, 17:00 UTC). This latter night time peak is slightly more pronounced at elevations below 3,000 m ASL, where diurnal variations are in general smaller compared to the TP.

To derive additional properties of dominant precipitation patterns, we also examined seasonal variations of convective and extreme precipitation. The results reveal that relative contributions of convective and extreme precipitation (90th percentile of daily precipitation) peak in July and follow the same seasonal curve as for total precipitation. However, convective precipitation over the TP contributes only up to 30% to the total summer precipitation, whereas more than 70% of the total summer precipitation amount is produced by the 90th percentile of daily rain rates. Hence, it could be concluded that a significant part of extreme precipitation are of non-convective type.

The two main questions, which have to be addressed in further precipitation studies on the TP are hence (a) the role of convection and (b) the role of the westerly circulation and other synoptic systems, which affect the TP between October and April. Due to the inherent limitations of satellite observations over the TP, we also conclude that cloud and precipitation retrievals for the specific environment of the TP need to be validated and improved based on ground radar measurements, in order to create a more robust climatology and to reliably relate the latter to convective processes.

ACKNOWLEDGEMENTS

This research was part of the Swedish National strategic research programs BECC and MERGE. The Strategic Priority Research Program of Chinese Academy of Sciences (XDA2006040103), M.W. is supported by Ministry of Science and Technology of China (2017YFA0604002), by the

National Natural Science Foundation of China (No. 41575073, 41621005 and 91744208). The Swedish National Space Agency, Grant/Award Number: SNSA: 188/18 4, The Swedish Research Council (2014–5320 and 2017–03780), The Swedish Foundation for International Cooperation in Research and Higher Education (CH2015-6226).

CONFLICT OF INTEREST

The authors declare no conflicts of interest.

ORCID

Deliang Chen  <https://orcid.org/0000-0003-0288-5618>

REFERENCES

- Bao, X., Zhang, F. and Sun, J. (2011) Diurnal variations of warm-season precipitation east of the Tibetan plateau over China. *Monthly Weather Review*, 139, 2790–2810.
- Beck, H.E., Van Dijk, A.I., Levizzani, V., Schellekens, J., Gonzalez Miralles, D., Martens, B. and De Roo, A. (2017) Mswep: 3-hourly 0.25 global gridded precipitation (1979–2015) by merging gauge, satellite, and reanalysis data. *Hydrology and Earth System Sciences*, 21, 589–615.
- Bibi, S., Wang, L., Li, X., Zhou, J., Chen, D. and Yao, T. (2018) Climatic and associated cryospheric, biospheric, and hydrological changes on the tibetan plateau: a review. *International Journal of Climatology*, 38, e1–e17.
- Casella, D., Panegrossi, G., Sanò, P., Marra, A.C., Dietrich, S., Johnson, B.T. and Kulie, M.S. (2017) Evaluation of the gpm-dpr snowfall detection capability: comparison with cloudsat-cpr. *Atmospheric Research*, 197, 64–75.
- Chen, D., Tian, Y., Yao, T. and Ou, T. (2016) Satellite measurements reveal strong anisotropy in spatial coherence of climate variations over the Tibet plateau. *Scientific Reports*, 6, 30304.
- Chen, D., Xu, B., Yao, T., Guo, Z., Cui, P., Chen, F., Zhang, R., Zhang, X., Zhang, Y., Fan, J., Hou, Z. and Zhang, T. (2015) Assessment of past, present and future environmental changes on the Tibetan plateau. *Chinese Science Bulletin*, 60, 3025–3035.
- Cuo, L. and Zhang, Y. (2017) Spatial patterns of wet season precipitation vertical gradients on the tibetan plateau and the surroundings. *Scientific Reports*, 7, 5057.
- Curio, J. and Scherer, D. (2016) Seasonality and spatial variability of dynamic precipitation controls on the tibetan plateau. *Earth System Dynamics*, 7, 767–782.
- Elsaesser, G.S. and Kummerow, C.D. (2015) The sensitivity of rainfall estimation to error assumptions in a bayesian passive microwave retrieval algorithm. *Journal of Applied Meteorology and Climatology*, 54, 408–422.
- Feng, X., Liu, C., Rasmussen, R. and Fan, G. (2014) A 10-yr climatology of tibetan plateau vortices with ncep climate forecast system reanalysis. *Journal of Applied Meteorology and Climatology*, 53, 34–46.
- Flohn, H. and Reiter, E.R. (1968) Contributions to a meteorology of the Tibetan Highlands. *Atmospheric science paper; no. 130*.
- Fu, Y. and Liu, G. (2007) Possible misidentification of rain type by trmm pr over tibetan plateau. *Journal of Applied Meteorology and Climatology*, 46, 667–672.

- Fujinami, H., Nomura, S. and Yasunari, T. (2005) Characteristics of diurnal variations in convection and precipitation over the southern Tibetan plateau during summer. *Scientific Online Letters on the Atmosphere Sola*, 1, 49–52.
- Gao, Y. and Liu, M. (2013) Evaluation of high-resolution satellite precipitation products using rain gauge observations over the Tibetan plateau. *Hydrology & Earth System Sciences*, 17, 837.
- Gao, Y., Xu, J. and Chen, D. (2015) Evaluation of wrf mesoscale climate simulations over the tibetan plateau during 1979–2011. *Journal of Climate*, 28, 2823–2841.
- Hou, A.Y., Kakar, R.K., Neeck, S., Azarbarzin, A.A., Kummerow, C. D., Kojima, M., Oki, R., Nakamura, K. and Iguchi, T. (2014) The global precipitation measurement mission. *Bulletin of the American Meteorological Society*, 95, 701–722.
- Hu, L., Deng, D., Gao, S. and Xu, X. (2016) The seasonal variation of tibetan convective systems: satellite observation. *Journal of Geophysical Research: Atmospheres*, 121, 5512–5525.
- Hu, L., Deng, D., Xu, X. and Zhao, P. (2017) The regional differences of tibetan convective systems in boreal summer. *Journal of Geophysical Research: Atmospheres*, 122, 7289–7299.
- Huffman, G.J., Bolvin, D.T., Braithwaite, D., Hsu, K., Joyce, R., Xie, P. and Yoo, S.-H. (2015a) Nasa global precipitation measurement (gpm) integrated multi-satellite retrievals for gpm (imerg). *Algorithm theoretical basis document, version, 4*, 30.
- Huffman, G.J., Bolvin, D.T. and Nelkin, E.J. (2015b) Integrated multi-satellite retrievals for gpm (imerg) technical documentation. *NASA/GSFC Code*, 612, 47.
- Iguchi, T., Seto, S., Meneghini, R., Yoshida, N., Awaka, J. and Kubota, T. (2010) Gpm/dpr level-2 algorithm theoretical basis document. *NASA Goddard Space Flight Center, Greenbelt, MD, USA, Tech. Rep.*
- Joyce, R.J., Janowiak, J.E., Arkin, P.A. and Xie, P. (2004) Cmorph: a method that produces global precipitation estimates from passive microwave and infrared data at high spatial and temporal resolution. *Journal of Hydrometeorology*, 5, 487–503.
- Kukulies, J., Chen, D. and Wang, M. (2019) Temporal and spatial variations of convection and precipitation over the Tibetan plateau based on recent satellite observations. Part i: cloud climatology derived from cloudsat and calipso. *International Journal of Climatology*, 39, 5396–5412.
- Kulie, M.S. and Bennartz, R. (2009) Utilizing spaceborne radars to retrieve dry snowfall. *Journal of Applied Meteorology and Climatology*, 48, 2564–2580.
- Kummerow, C., Barnes, W., Kozu, T., Shiue, J. and Simpson, J. (1998) The tropical rainfall measuring mission (trmm) sensor package. *Journal of Atmospheric and Oceanic Technology*, 15, 809–817.
- Kummerow, C., Hong, Y., Olson, W., Yang, S., Adler, R., McCollum, J., Ferraro, R., Petty, G., Shin, D.-B. and Wilhelm, T. (2001) The evolution of the Goddard profiling algorithm (gprof) for rainfall estimation from passive microwave sensors. *Journal of Applied Meteorology*, 40, 1801–1820.
- Li, X., Wang, L., Guo, X. and Chen, D. (2017) Does summer precipitation trend of Tibetan plateau depend on elevation? *International Journal of Climatology*, 37, 1278–1284.
- Li, Y., Yun, W., Yang, S., Liang, H., Shouting, G. and Fu, R. (2008) Characteristics of summer convective systems initiated over the Tibetan plateau. Part i: origin, track, development, and precipitation. *Journal of Applied Meteorology and Climatology*, 47, 2679–2695.
- Liang, H., Yang, S., Li, Y.D. and Gao, S.T. (2010) Diurnal variability of precipitation depth over the Tibetan plateau and its surrounding regions. *Advances in Atmospheric Sciences*, 27, 115–122.
- Lin, C., Chen, D., Yang, K. and Ou, T. (2018) Impact of model resolution on simulating the water vapor transport through the central himalayas: implication for models' wet bias over the Tibetan plateau. *Climate Dynamics*, 51, 3195–3207.
- Liu, W., Wang, L., Chen, D., Tu, K., Ruan, C. and Hu, Z. (2016) Large-scale circulation classification and its links to observed precipitation in the eastern and central Tibetan plateau. *Climate Dynamics*, 46, 3481–3497.
- Luo, H. and Yanai, M. (1983) The large-scale circulation and heat sources over the Tibetan plateau and surrounding areas during the early summer of 1979. Part i: precipitation and kinematic analyses. *Monthly Weather Review*, 111, 922–944.
- Ma, Y., Yang, Y., Han, Z., Tang, G., Maguire, L., Chu, Z. and Hong, Y. (2018) Comprehensive evaluation of ensemble multi-satellite precipitation dataset using the dynamic bayesian model averaging scheme over the tibetan plateau. *Journal of Hydrology*, 556, 634–644.
- Maddox, R.A. (1980) Mesoscale convective complexes. *Bulletin of the American Meteorological Society*, 61, 1374–1387.
- Maussion, F., Scherer, D., Moelg, T., Collier, E. and Curio, J. (2014) Precipitation seasonality and variability over the Tibetan plateau as resolved by the high Asia reanalysis. *Journal of Climate*, 27, 1910–1927.
- Su, F., Duan, X., Chen, D., Hao, Z. and Cuo, L. (2013) Evaluation of the global climate models in the cmip5 over the Tibetan plateau. *Journal of Climate*, 26, 3187–3208.
- Sungmin, O., Kirstetter, P.-E. (2018) Evaluation of diurnal variation of gpm imerg-derived summer precipitation over the contiguous us using mrms data. *Quarterly Journal of the Royal Meteorological Society*, 144, 270–281.
- Sugimoto, S. and Ueno, K. (2010) Formation of mesoscale convective systems over the eastern tibetan plateau affected by plateau-scale heating contrasts. *Journal of Geophysical Research: Atmospheres*, 115.
- Tang, G., Ma, Y., Long, D., Zhong, L. and Hong, Y. (2016) Evaluation of gpm day-1 imerg and tpm version-7 legacy products over mainland China at multiple spatiotemporal scales. *Journal of Hydrology*, 533, 152–167.
- Tong, K., Su, F., Yang, D., Zhang, L. and Hao, Z. (2014) Tibetan plateau precipitation as depicted by gauge observations, reanalyses and satellite retrievals. *International Journal of Climatology*, 34, 265–285.
- Wang, Y., Yang, K., Pan, Z., Qin, J., Chen, D., Lin, C., Chen, Y., Lazhu, Tang, W., Han, M., Lu, N. and Wu, H. (2017) Evaluation of precipitable water vapor from four satellite products and four reanalysis datasets against GPS measurements on the southern Tibetan plateau. *Journal of Climate*, 30, 5699–5713.
- Xu, R., Tian, F., Yang, L., Hu, H. and Lu, H. (2017) Ground validation of gpm imerg and trmm 3b42v7 rainfall products over southern Tibetan plateau based on a high-density rain-gauge network. *Journal of Geophysical Research Atmospheres*, 122, 910–924.
- Xu, W. and Zipser, E.J. (2011) Diurnal variations of precipitation, deep convection, and lightning over and east of the eastern Tibetan plateau. *Journal of Climate*, 24, 448–465.

- Yao, T., Masson-Delmotte, V., Gao, J., Yu, W., Yang, X., Risi, C., Sturm, C., Werner, M., Zhao, H., He, Y., Ren, W., Tian, L., Shi, C. and Hou, S. (2013) A review of climatic controls on $\delta^{18}O$ in precipitation over the Tibetan plateau: observations and simulations. *Reviews of Geophysics*, 51, 525–548.
- Yao, T., Xue, Y., Chen, D., Chen, F., Thompson, L., Cui, P., Koike, T., Lau, W.K.-M., Lettenmaier, D., Mosbrugger, V., et al. (2018) Recent third pole's rapid warming accompanies cryospheric melt and water cycle intensification and interactions between monsoon and environment: multi-disciplinary approach with observation, modeling and analysis. *Bulletin of the American Meteorological Society*, 100, 423–444.
- Yihui, D. and Chan, J.C. (2005) The east asian summer monsoon: an overview. *Meteorology and Atmospheric Physics*, 89, 117–142.
- You, Q., Min, J., Zhang, W., Pepin, N. and Kang, S. (2015) Comparison of multiple datasets with gridded precipitation observations over the tibetan plateau. *Climate Dynamics*, 45, 791–806.
- Zhang, C., Tang, Q. and Chen, D. (2017) Recent changes in the moisture source of precipitation over the Tibetan plateau. *Journal of Climate*, 30, 1807–1819.
- Zhang, Y., Sun, J. and Fu, S. (2014) Impacts of diurnal variation of mountain-plain solenoid circulations on precipitation and vortices east of the Tibetan plateau during the mei-yu season. *Advances in Atmospheric Sciences*, 31, 139–153.
- Zhou, T., Yu, R., Chen, H., Dai, A. and Pan, Y. (2008) Summer precipitation frequency, intensity, and diurnal cycle over China: a comparison of satellite data with rain gauge observations. *Journal of Climate*, 21, 3997–4010.

How to cite this article: Kukulies J, Chen D, Wang M. Temporal and spatial variations of convection, clouds and precipitation over the Tibetan Plateau from recent satellite observations. Part II: Precipitation climatology derived from global precipitation measurement mission. *Int J Climatol*. 2020;1–18. <https://doi.org/10.1002/joc.6493>